ASME Journal of Heat and Mass Transfer
Online journal at:
https://asmedigitalcollection.asme.org/heattransfer

A Transformative Approach for Breast Cancer Detection Using Physics-Informed Neural Network and Surface Temperature Data

Isaac Perez-Raya
Mechanical Engineering Department,
Rochester Institute of Technology,
Rochester, NY 14618;
BiRed Imaging,
Rochester, NY 14604,
e-mails: ibpeme@rit.edu;
iperez@biredimaging.com

Carlos Gutierrez
Mechanical Engineering Department,
Rochester Institute of Technology,
Rochester, NY 14618

Satish Kandlikar[1]
Mechanical Engineering Department,
Rochester Institute of Technology,
Rochester, NY 14618;
BiRed Imaging,
Rochester, NY 14604,
e-mails: sgkeme@rit.edu;
skandlikar@biredimaging.com

Early detection is the most effective defense against breast cancer. Mammography is a well-established X-ray-based technique that is used for annual or biennial screening of women above age of 40. Since the dense breast tissue sometimes obscures the cancer in an X-ray image, about 10% of screened women are recalled and undergo additional adjunctive modalities, such as ultrasound, digital breast tomosynthesis, or magnetic resonance imaging. These modalities have drawbacks such as additional radiation dosage, overdiagnosis, and high cost. A new concurrent multispectral imaging approach was recently presented to eliminate the high recall rates by utilizing the breast surface temperature data with an inverse physics-informed neural network algorithm. This method utilizes the bioheat transfer modeling as the governing physics equations and conducted inverse heat transfer modeling using infrared temperatures to predict the presence of a tumor heat source. Validation of the predicted tumor size and location was conducted on a biopsy-proven breast cancer patient using infrared temperature data captured of the breast surface and pathology reports. A regression analysis between the predicted temperatures and infrared temperatures showed a coefficient of determination of 0.98. The absolute error in the predicted tumor size was 0.4 cm and the maximum absolute error in tumor location was 0.3 cm. The proposed approach shows promising results and performance. However, additional testing with more patients is required to quantify the standard deviation in the prediction and establish the sensitivity and specificity of the machine learning technique.
[DOI: 10.1115/1.4065673]

1 Introduction

It is well documented that breast cancer is a leading cause of mortality in women [1–3]. The large-scale network developed to routinely screen women over age of 40, annually or biannually, is credited with a dramatic reduction of mortality rate from breast cancer over last two decades [4]. Mammography involves compressing a breast between two plates and taking X-ray images of the flattened breast. The compression causes discomfort, and as a result, some women tend to avoid mammograms. This reduces the effectiveness of the overall screening paradigm.

Further, mammography is unable to detect a tumor if it appears behind dense breast tissue, which has a masking effect in an X-ray image. To improve cancer detection rate, patients with mammograms that appear suspicious are recalled for additional adjunctive screening. A higher recall rate not only captures a higher number of cancer cases, but it also results in a large number of false positive cases, which undergo additional adjunctive screening. It also results in a large number of patients undergoing biopsy to arrive at a conclusive diagnosis. In addition to the high cost of biopsy, the procedure is very painful and causes severe disruptions in lactating mothers. Although it varies among different hospitals, a recall rate of 10% is recommended after mammograms [5]; however, only 0.4% of women screened have cancer from the historical screening data [6]. Considering 48×10^6 women are screened every year in the US, estimated 9.6% or 4.61×10^6 women who do not have cancer undergo additional screening and biopsy following recalls.

The false positive outcomes increase the healthcare costs. In addition, the recall, followed by additional screening, takes a high psychological toll [7]. The immediate anxiety, as well as the long-term fear of mammography, causes some women to avoid mammography afterwards. The search for new adjunctive technologies that are harmless, avoid breast compression, and have a low false-positive rate is an area of active research.

Cancer is associated with tumors that have a higher metabolic rate and a higher perfusion rate in the region surrounding the tumor and act as a heat source. The normal heat transfer mode from the chest wall to the breast surface is altered due to the presence of the heat source within the breast and the temperatures on the breast surface are altered. Using an inverse heat transfer modeling approach and treating a tumor as a heat source, numerical techniques have been developed to solve the underlying governing equations to predict the presence of cancer, or malignancy, from the breast surface temperature data [8–10]. These models require numerical solution of heat transfer equations at a large number of discrete points on the surface as well as inside of the breast in an inverse algorithm that utilizes an iterative process. Gonzalez-Hernandez et al. [8] and Gutierrez et al. [10] utilized regions of interest in their inverse detection algorithms to improve efficiency, but still required large

[1]Corresponding author.

Contributed by the Heat Transfer Division of ASME for publication in the Journal of Heat and Mass Transfer. Manuscript received November 10, 2023; final manuscript received May 22, 2024; published online June 17, 2024. Assoc. Editor: Antonio Jose Silva Neto.

data points to numerically solve the heat transfer equations. There is a need for an efficient physics-based inverse heat transfer approach for detecting the presence of malignant breast cancer. This is accomplished efficiently in a physics-informed neural networks (PINN) algorithm, which is discussed in greater detail in the present paper.

The surface temperature data needed in the PINN model can be obtained with a highly sensitive infrared camera. The use of infrared cameras is well accepted in the medical community as it is widely used for body temperature measurements in doctors' offices, hospitals, as well as in airports and malls for detection of COVID-19, for example. These cameras are equipped with advanced computer algorithms to predict deep body temperature from the measurement of forehead temperatures. Similarly, the breast surface temperatures can be measured accurately with a highly sensitive (20 mK, or better) infrared camera and the temperatures are registered at discrete points on the breast surface obtained from a digital breast model using three-dimensional (3D) image reconstruction techniques. The detection of breast cancer using surface temperature data from infrared images, 3D image reconstructed models, and physics-based inverse heat transfer approaches has shown great promise [8–10]. Inverse heat transfer modeling using PINN has shown great promise in the field of heat transfer [11–14]. However, there have been very few studies that have utilized PINN with inverse problems in bioheat transfer applications. Perez-Raya and Kandlikar [15] introduced an inverse PINN method to predict thermal properties of breast cancer.

The current work presents a brief literature review on PINN modeling utilized in forward and inverse heat transfer modeling, as well as a developed inverse PINN algorithm for breast cancer detection. The novelty of the developed algorithm is its ability to detect breast cancer from IR surface temperature data using inverse heat transfer PINN modeling and bioheat transfer modeling. In addition, this work shows the validation of the algorithm with clinical data of a biopsy-proven breast cancer patient.

2 Recent Developments in Physics-Informed Neural Networks Modeling

Physics-informed neural networks have played a major role in advancing computational modeling of physics-based problems using governing physics laws with machine learning techniques [16,17]. PINNs were first coined by Raissi et al. [18–23] for solving ordinary differential equations (ODEs) and partial differential equations (PDEs) using machine learning techniques. This was useful as the governing equations that make up various physics-based problems are typically in the form of ODEs and PDEs. The concept of solving ODEs and PDEs using machine learning can be traced back to the work by Dissanayake and Phan-Thien [24], and Lagaris et al. [25,26], where the authors utilized artificial neural networks. This section will describe the concepts and fundamental structure of PINNs as well as give a brief literature survey of PINNs utilized in heat transfer and biomedical applications.

2.1 Physics-Informed Neural Networks Forward and Inverse Modeling. According to Kollmansberger et al. [17], neural networks (NNs) are parameterized functions that define mappings between an input $\boldsymbol{x}$ and prediction output $\boldsymbol{y}$ through various layers of mappings such that:

$$\begin{aligned} \boldsymbol{z}^{(0)} &= \boldsymbol{x} \\ \boldsymbol{z}^{(1)} &= h_1\left(\boldsymbol{W}^{(1)}\boldsymbol{z}^{(0)} + \boldsymbol{b}^{(1)}\right) \\ &\vdots \\ \boldsymbol{z}^{(k)} &= h_k\left(\boldsymbol{W}^{(k)}\boldsymbol{z}^{(k-1)} + \boldsymbol{b}^{(k)}\right) \\ &\vdots \\ \boldsymbol{z}^{(L)} &= h_L\left(\boldsymbol{W}^{(L)}\boldsymbol{z}^{(L-1)} + \boldsymbol{b}^{(L)}\right) \\ \tilde{\boldsymbol{y}}_{\boldsymbol{W}} &= f\left(\boldsymbol{W}^{(L+1)}\boldsymbol{z}^{(L)}\right) \end{aligned} \tag{1}$$

where k is the NN layer index going from $k = 1, 2, \ldots, L$, $\boldsymbol{W}^k$ are weight parameters at layer k learned by the NNs to obtain $\tilde{\boldsymbol{y}}_{\boldsymbol{W}}$, $\boldsymbol{b}^k$ are bias factors at layer k add to the NN in the absence of an input and may be obtained from expected values associated with training to obtain $\tilde{\boldsymbol{y}}_{\boldsymbol{W}}$, $h_k(\cdot)$ are activation functions in one of the layers of an NN, $\boldsymbol{z}^k$ are the outputs of each layer k obtained from the activation function, and $f(\cdot)$ is the model used to approximate or predict the output $\tilde{\boldsymbol{y}}_{\boldsymbol{W}}$. This NN model has an input layer (0^{th} layer), L hidden layers, and an output layer ($L + 1$ layer). Figure 1 shows a depiction of the NN model as well as the machine learning flowchart process for obtaining a final prediction from the input or testing data. The output is predicted through iteratively optimizing the weights $\boldsymbol{W}$ using a loss function $L(\boldsymbol{W})$ and labeled or training data through the following:

$$L(\boldsymbol{W}) = \|\boldsymbol{Y} - \tilde{\boldsymbol{y}}_{\boldsymbol{W}}\|_2^2 \tag{2}$$

$$\boldsymbol{W}_{i+1} = \boldsymbol{W}_i - \eta \cdot \nabla_{\boldsymbol{W}} L(\boldsymbol{W}) \tag{3}$$

where $\boldsymbol{Y}$ is the labeled data, i is the iteration index, η is a learning rate parameter utilized in machine learning techniques, and $\nabla_{\boldsymbol{W}}$ is the gradient with respect to the weights. The optimizer shown in Fig. 1 checks if $L(\boldsymbol{W})$ is minimized with the current weight and if not utilizes Eq. (3) to update the weight. In machine learning, it is common to use these gradient-based techniques, such as the one from Eq. (3), as optimizers [27–29]. Utilizing prior knowledge or labeled data associated with the output to learn the weights is called supervised learning. In unsupervised learning, this label data is not available and the data have to learn through patterns based on a larger input dataset [16,17,27–29].

In physics-based problems, PINNs utilize the NN model and the machine learning structure to conduct forward and inverse problems [16,17]. Figure 2 shows an example of a forward and an inverse problem PINN structure for the following transient heat conduction problem:

$$\rho c_p \frac{\partial T}{\partial t} = k\nabla T, \quad \boldsymbol{x} \in \Omega,\ t > 0 \tag{4}$$

$$T(\boldsymbol{x}, t) = T_c, \quad \boldsymbol{x} \in \partial\Omega,\ t > 0 \tag{5}$$

$$k\frac{\partial T}{\partial \boldsymbol{n}}(\boldsymbol{x}, t) = q_c, \quad \boldsymbol{x} \in \partial\Omega,\ t > 0 \tag{6}$$

$$T(\boldsymbol{x}, 0) = T_0, \quad \boldsymbol{x} \in \Omega \tag{7}$$

where ρ is the density, c_p is the specific heat, T is the temperature, k is the thermal conductivity, t is time, $\boldsymbol{x}$ is the spatial coordinates (x, y, z), Ω is the domain, $\partial\Omega$ is the boundary of the domain, and $\boldsymbol{n}$ is the normal vector of the boundary points. The input for PINNs is the computational domain Ω of the physical system under study in terms of spatiotemporal data (x, y, z, t) or $(\boldsymbol{x}, t)$. Machine learning NN models utilize the concept of automatic differentiation to conduct back propagation techniques in NNs. PINNs utilize automatic differentiation on the output of the NN model to conduct forward modeling based on the governing equation (Eq. (4)), boundary conditions (Eqs. (5) and (6)), and initial condition (Eq. (7)). These equations and conditions are utilized as loss functions

$$L_{\text{Eq}} = \rho c_p \frac{\partial \tilde{T}}{\partial t} - k\nabla\tilde{T} \tag{8}$$

$$L_{\text{BC},1} = \tilde{T} - T_c \tag{9}$$

$$L_{\text{BC},2} = k\frac{\partial \tilde{T}}{\partial \boldsymbol{n}} - q_c \tag{10}$$

$$L_{\text{BC}} = L_{\text{BC},1} + L_{\text{BC},2} \tag{11}$$

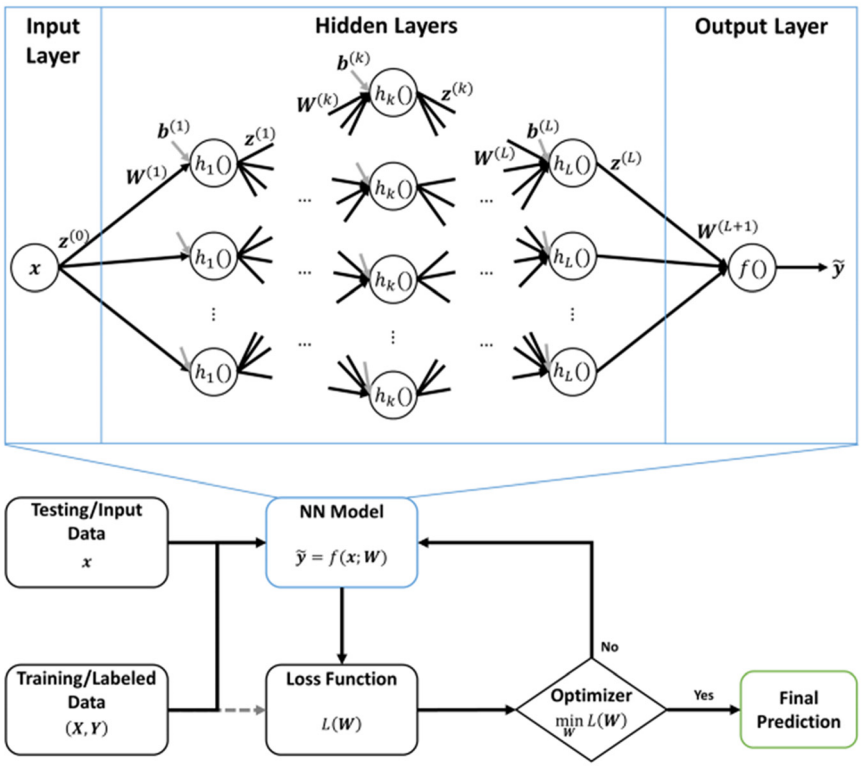

Fig. 1 Top: Illustration of neural network (NN) model with an input layer, hidden layers, and an output layer. Bottom: Flowchart of a machine learning process that utilizes an NN model to obtain a final prediction from the testing/input data using training/labeled data and optimization of a loss function.

$$L_{\text{IC}} = \tilde{T} - T_0 \tag{12}$$

$$L_{\text{Fwd}} = L_{\text{Eq}} + L_{\text{BC}} + L_{\text{IC}} \tag{13}$$

where $\tilde{T}$ is the predicted temperature from the PINN, L_{Eq} is the loss from the governing equation (Eq. (4)), L_{BC} is the loss from the boundary conditions (Eqs. (5) and (6)), L_{IC} is the loss from the initial condition (Eq. (7)), and L_{Fwd} is the total loss from the forward problem. For forward problems, the standard PINN models utilize unsupervised learning wherein there is no prior knowledge or available known data of the system under study. In this case, the loss function $L(\boldsymbol{W}) = L_{\text{Fwd}}$. When data are available, a supervised learning model is utilized by adding a loss based on the known data L_{Data} such that

$$L(\boldsymbol{W}) = L_{\text{Fwd}} + L_{\text{Data}} \tag{14}$$

$$L_{\text{Data}} = \tilde{T} - T_{\text{Data}} \tag{15}$$

where T_{Data} is the known data. The loss function then goes to the optimizer to obtain the weights that will give a final predicted temperature distribution $\boldsymbol{T}_{\text{pred}}$. In the forward PINN model, the system parameters, governing equations, boundary conditions, and initial conditions are known to aid in predicting the final physics distribution model. This is not the case for inverse PINN modeling as some information may not be known such as the thermal conductivity for the forward model example shown in Fig. 2. Supervised learning is utilized by using known temperature data T_{Data} at specific locations to predict the thermal conductivity k_{pred}. Figure 2 serves as a representation of a PINN utilized in forward and inverse modeling of the transient heat conduction problem (Eqs. (4)–(7)). This is utilized as a guide for developing a PINN model that is dependent on the application by changing the governing equations, system parameters, and known data. Similar models have been shown in Refs. [16,17,30,31].

2.2 Heat Transfer Applications. The application of machine learning techniques to heat transfer problems was first explored by Jambunathan et al. [32]. The authors utilized artificial neural networks to predict the heat transfer coefficient in a one-dimensional transient heat conduction problem using data samples from known solutions. This inspired many researchers to implement machine learning techniques such as PINNs on heat transfer problems. A summary of current works that have utilized PINN for forward modeling on heat transfer problems is shown in Table 1. Table 1 shows the heat transfer problem type that was solved, the variables predicted by the PINN model, the known data provided to the PINN model, and the prediction errors when comparing to traditional computational fluid dynamics (CFD) methods. The table covers natural and forced convection problems [11,33,34], heat conduction problems [14,34,35], and bioheat transfer in breast cancer problems [15,36]. The first two convection problems [11,33] and the last two heat conduction problems [14,35] utilize supervised learning techniques to conduct forward problems using PINNs. This technique utilizes the known data at specified locations to train the weights of the PINN. The other convection and conduction problems [14,34] utilized the standard unsupervised learning PINN model that used the governing equations, boundary conditions, and initial conditions in the learning. The two bioheat transfer problems [15,36] in Table 1 are the only ones that have tackled bioheat modeling of breast cancer using unsupervised forward PINN modeling. In comparison to standard CFD models, both the supervised and unsupervised PINN models show promising results when looking at the relative errors E_{Rel} and absolute errors E_{Abs} reported by the authors. This shows the capability of utilizing PINNs for accurate forward modeling of heat transfer applications and indicates further extension into bioheat applications.

In addition to solving forward problems in heat transfer applications, current studies have researched the use of PINNs to solve inverse heat transfer problems. Table 2 shows a summary of current studies that have utilized PINNs for inverse problems in heat transfer applications similar to Table 1. Also, Table 2 covers

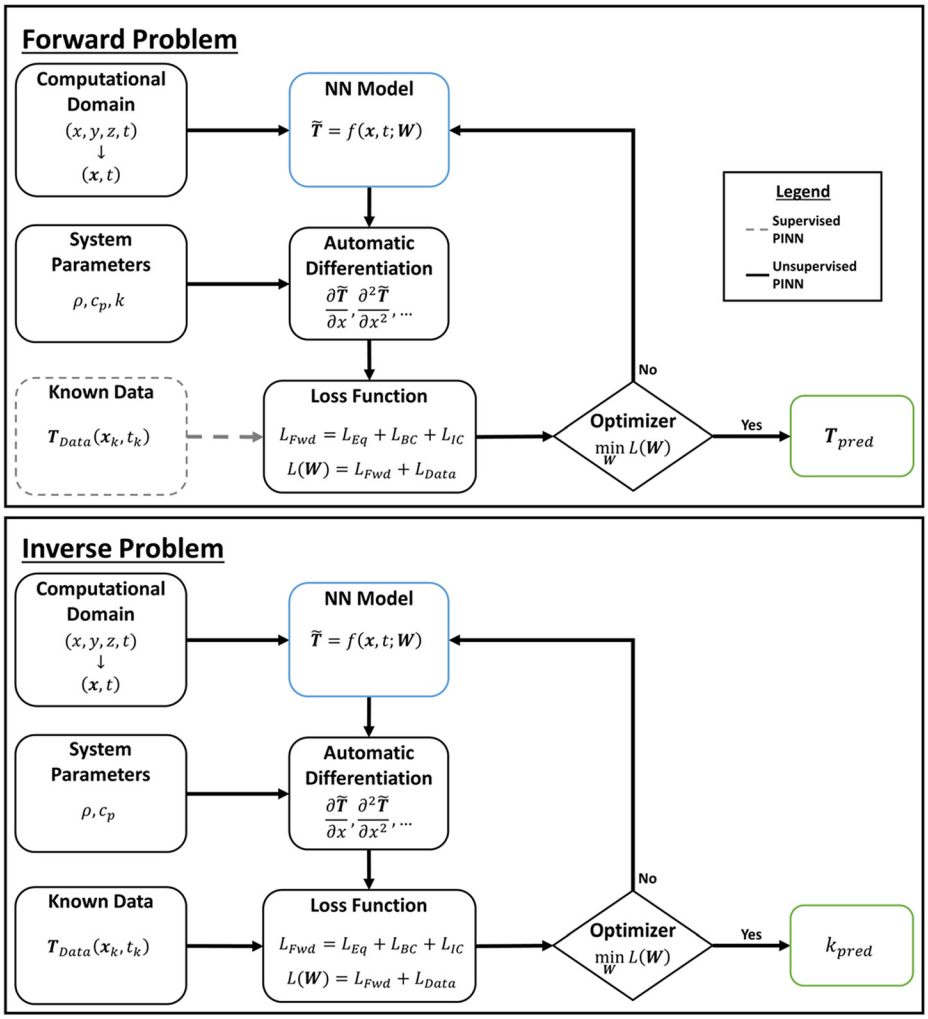

Fig. 2 Top: Example flowchart of PINN model utilized to solve a forward transient heat conduction problem (Eqs. (4)–(7)) to predict the temperature distribution using the computational domain, system parameters, automatic differentiation, and optimization of the loss function through unsupervised learning or supervised learning using known data. Bottom: Example flowchart of PINN model utilized to solve an inverse transient heat conduction problem that utilizes supervised learning through known temperature data to predict the thermal conductivity from known temperature data.

concepts in two-phase heat transfer [11], heat conduction [12,14], natural and forced convection [12], heat radiation [12,13], and bioheat transfer [15]. The goal of the authors in these works is to obtain thermal properties [11–13,15], boundary conditions [14], and heat sources [12] through the governing equations, conditions, and known data. The error in prediction compares the predicted value with ground truth data, which show the ability of PINNs to accurately predict properties regardless of the difficulty of the problem. The three prediction error metrics shown in Table 2 are the relative error E_{Rel}, absolute error E_{Abs}, and percent error E_{per}. In the two-phase heat Stefan problem [11], the authors were able to obtain the thermal diffusivity constant for each phase using known temperature data at specific points. This was in addition to forward modeling the two-phase Stefan problem and obtaining the temperature distribution and latent moving interface, which would be difficult in traditional CFD methods. This shows the capability of PINNs being utilized in various inverse heat transfer problems accurately by using measured data at specified locations. In the application of bioheat transfer in breast cancer, Perez-Raya and Kandlikar [15] showed that the thermal conductivity of breast tissue can be obtained using the breast surface temperatures.

2.3 Biomedical Applications Using Patient Data. Machine learning and artificial intelligence have been extensively utilized in solving biomedical and healthcare-related problems [29,37,38]. In traditional physics-based numerical modeling, patient data are utilized to generate computational domains, provide physical properties, or provide physics constraints for conducting numerical simulations. In current studies, PINNs have been utilized extensively in biomedical applications to solve hemodynamics forward and inverse problems using patient data [39–45]. Some studies utilized timeseries and flow data from patient data to study blood flow using PINNs [39,44,45]. Others have utilized patient-specific geometries with timeseries and flow data generated from patient data, such as magnetic resonance imaging (MRI) or other imaging modalities, to study the blood flow using PINNs [39–41,43,46]. This shows the capability of PINNs to work with patient data to solve complex problems in biomedical applications.

3 Developing an Inverse Physics-Informed Neural Networks Algorithm for Breast Cancer Detection

Increased metabolic activity of a tumor in the breast alters the temperature field providing the breast surface temperature as a sense

Table 1 Applications of PINNs to forward problems in heat transfer applications

Problem type	Predicted variables	Known data	Prediction error
Flow past a cylinder [11]	θ - Temperature V - Velocity P - Pressure	θ_{Data} at various points	$E_{\text{Rel},\theta}$: 0.73%
2D convection in a rotating porous medium [33]	Ψ – Stream function V – Velocity T – Temperature	Low fidelity T_{Data}	$E_{\text{Abs},T}$: 1.3×10^{-4}
Conjugate natural convection [34]	θ_{s1} - Temperature at solid domain 1 θ_f - Temperature at fluid domain θ_{s2} - Temperature at solid domain 2 V - Fluid velocity p - Fluid pressure	None	$E_{\text{Abs},\theta}$: 2×10^{-2}
2D heat conduction with nonlinear heat source and nonuniform thermal conductivity [34]	θ_1 - Temperature at domain 1 θ_2 - Temperature at domain 2 θ_3 - Temperature at domain 3	None	$E_{\text{Abs},\theta}$: 1×10^{-2}
2D heat conduction over a two-layered eccentric cylinder [14]	T - Temperature	None	$E_{\text{Rel},T}$: 4.02×10^{-5}
3D heat conduction over a two-layered cube [14]	T - Temperature	None	$E_{\text{Rel},T}$: 5×10^{-5}
1D bar with a given boundary heat flux (transient heat conduction) [35]	T - Temperature q - Input heat flux	T_{Data}	$E_{\text{Rel},T}$: 1.208×10^{-3}
2D plate with unknown body heat flux (transient heat conduction) [35]	T - Temperature q - Input heat flux	T_{Data} q_{Data}	$E_{\text{Rel},T}$: 2.398×10^{-2}
Bioheat modeling of breast cancer in patient-specific breast models [15]	T - Temperature	None	$E_{\text{Abs},T}$: 0.3
Bioheat modeling of breast cancer in a hemispherical breast model [36]	T - Temperature	None	Not reported

Table 2 Applications of PINNs to inverse problems in heat transfer applications

Problem type	Predicted variables	Known data	Prediction error
Two-phase Stefan problems [11]	u - temperature distribution s - latent moving interface k_1 - thermal diffusivity of phase 1 k_2 - thermal diffusivity of phase 2	T_{Data}	E_{Abs,k_1}: 3×10^{-3} E_{Abs,k_2}: 0.0
Inverse problem of 2D heat conduction over a two-layered cylinder [14]	T - Temperature	Sparse boundary T_{Data}	$E_{\text{Rel},T}$: 5×10^{-3}
Transient heat conduction [12]	θ - Temperature k_1 - thermal conductivity 1 k_3 - thermal conductivity 3	T_{Data}	E_{Abs,k_1}:8×10^{-4} E_{Abs,k_3}: 2.7×10^{-3}
Rectangular fin [12]	θ - Temperature m - surface heat transfer coefficient	T_{Data}	$E_{\text{Abs},m}$: 0.02
Annular fins [12]	T - Temperature h/k - convection to conduction ratio	T_{Data}	$E_{\text{Abs},h/k}$: 1×10^{-3}
Rectangular fin with heat generation [12]	T - Temperature G - Heat generation number	T_{Data}	$E_{\text{Abs},G}$: 4×10^{-4}
Porous fin subjected to radiative heat [12]	T - Temperature Q_0 - Heat generation number	T_{Data}	E_{Abs,Q_0}: 5×10^{-4}
Vascular-based active-cooling of sine wave channel through a square domain [13]	θ - Temperature k - thermal conductivity	T_{Data}	$E_{\text{Per},k}$: 3.0%
Bioheat modeling of breast cancer in patient-specific breast models [15]	T - Temperature k - thermal conductivity	Breast surface temperatures	$E_{\text{Per},k}$: 6.5%

variable for detecting tumors. Bioheat transfer modeling through Pennes bioheat equation [47] has been utilized to conduct numerical modeling of breast cancer [48–52]. Studies have been conducted that have utilized bioheat transfer and inverse heat transfer modeling to detect a tumor heat source using IR temperatures and ANSYS FLUENT [8–10]. In this study, we demonstrate the use of a physics-informed neural network to detect heat sources with surface data (PINN-SDSD). The sources correspond to metabolic activity of a breast and can be identified from the breast surface temperatures measured by a highly sensitive infrared camera that works similar to an infrared thermometer used in clinical practice. Different from conventional machine learning models, the PINN model is patient-specific (meaning that the PINN model gets trained individually on each patient).

The PINN-SDSD model, consisting of a physics-informed fully connected neural network with optimized number of hidden layers and neurons, is trained to find the temperatures and the region of high heat generation (indicative of tumor presence) that satisfy the Pennes bioheat equation and the patient-specific IR temperatures. The neural network model has three hidden layers and twenty neurons on each layer, which is an optimal configuration to achieve an accurate solution of the Pennes bioheat equation in breast cancer thermal transport [15].

The optimizer minimizes the total loss loss_T given by:

Table 3 Thermal properties utilized for the simulation and tumor detection with the PINN-SDSD

Parameter	Value	Unit
Thermal conductivity (k) [53]	0.3	W/m-K
Perfusion rate of healthy tissue (ω_h) [53]	1.8×10^{-4}	1/s
Perfusion rate of tumor (ω_t) [53]	9×10^{-3}	1/s
Metabolic activity of healthy tissue ($\dot{q}_h$) [53]	450	W/m^3
Metabolic activity of tumor ($\dot{q}_t$) [53]	5000–70,000	W/m^3
Temperature of arteries (T_a) [54]	37	°C
Specific heat of blood (c_b) [54]	3840	J/kg-K
Density of blood (ρ_b) [54]	1060	Kg/m^3
Chest temperature (T_c) [53]	37	°C
Heat transfer coefficient (h) [52]	5	W/m^2-K
Ambient temperature (T_∞)	21	°C

$$\text{loss}_T = \frac{1}{N_{\text{inter}}}\sum_{i=1}^{N_{\text{inter}}}(\text{loss}_{\text{inter},i})^2 + \frac{1}{N_{\text{BC}}}\sum_{j=1}^{N_{\text{BC}}}(\text{loss}_{\text{BC},j})^2 \tag{16}$$

where N_{inter} and N_{BC} correspond to the number of interior and boundary points in the point-clouds, respectively. The term $\text{loss}_{\text{interEqs}}$ is calculated from the dimensionless Pennes bioheat model.

$$\text{loss}_{\text{inter},i} = \frac{\partial^2 T^*}{\partial x^{*2}} + \frac{\partial^2 T^*}{\partial y^{*2}} + \frac{\partial^2 T^*}{\partial z^{*2}} + \frac{\rho c}{k}\omega_b D^2 (T_a^* - T^*) + \frac{2D^2}{k(T_{\max} - T_{\min})}\dot{q}_m \tag{17}$$

where ω_b and $\dot{q}_m$ are expressed in terms of the tumor radius and location:

$$\omega_b = H\omega_{\text{tumor}} + (1-H)\omega_{\text{healthy}} \tag{18}$$

$$\dot{q}_m = H\dot{q}_{m\text{tumor}} + (1-H)\dot{q}_{m\text{healthy}} \tag{19}$$

H is an indicator function representing the distribution of the source. In the present work, H equal to 1 in the tumor region and 0 in the healthy region. Under the assumption of representing the tumor as a sphere of equivalent diameter, the indicator function is defined as:

$$\begin{aligned} H &= 1 \text{ if } (x-x_0)^2 + (y-y_0)^2 + (z-z_0)^2 \le d_0^2/4 \\ H &= 0 \text{ if } (x-x_0)^2 + (y-y_0)^2 + (z-z_0)^2 > d_0^2/4 \end{aligned} \tag{20}$$

where x_0, y_0, z_0, and d_0 are the coordinates of the tumor location and the tumor diameter.

Equation (21), derived by Gautherie [53], related the metabolic activity and tumor radius during the training of the PINN-SDSD.

$$\dot{q}_m = \frac{3.27 \times 10^6}{468.5\ln(100 d_0) + 50} \tag{21}$$

In Eqs. (17)–(21), T_a, $\dot{q}_m$, ω, ρ, c_p, k, and h, stand for artery blood temperature, metabolic heat generation, blood perfusion rate, tissue density, tissue-specific heat, tissue thermal conductivity, and ambient convective heat transfer coefficient respectively [47–49].

The term loss_{BC} accounting for the boundary is calculated from the boundary conditions of convection at the breast surface, constant body temperature at the body chest ($T = T_{\text{ch}}$),

$$\text{loss}_{\text{BC1},i} = \frac{k}{D}\frac{\partial T^*}{\partial n^*}\Big|_{\text{pred}} - h\left(T_\infty^* - T_{\text{pred}}^*\right) \tag{22}$$

$$\text{loss}_{\text{BC2},i} = T_{\text{ch}}^* - T_{\text{ch}}^* \tag{23}$$

$$\text{loss}_{\text{BC3},i} = T_{\text{surf}}^* - T_{\text{IR,denoised}}^* \tag{24}$$

By feeding Eqs. (16)–(24) to the optimizer, the inverse PINN adjusts the values of the tumor characteristics (x_0, y_0, z_0, d_0) to ensure a minimal loss.

Table 3 shows the thermal properties adopted. The patients were screened with the IR imaging system in an enclosed environment under ambient conditions.

The inputs consist of 1000 random surface data points $T_{\text{IR}}(x_s, y_s, z_s)$, 500 random chest points ($x_{\text{ch}}, y_{\text{ch}}, z_{\text{ch}}$), and 20,000 random interior points ($x_{\text{int}}, y_{\text{int}}, z_{\text{int}}$) for training. Figure 3 shows the spatial point-clouds for the identified key regions of (a) breast surface, (b) chest, and (c) interior. The digital breast model contains information on points coordinates over the surface and chest. The interior points were generated by creating a computational mesh from the digital breast model and extracting the points at the cell centers of the mesh. The points were randomly extracted from the surface or the computational mesh. The points distribute homogeneously with the same amount of points near the tumor region or breast surface. The PINN-SDSD receives these points as inputs without special sorting or arrangement.

4 Results

The results in the present section involved analyzing surface temperature data from a patient (patient-8) with a diagnosed breast tumor. The tumor is located at a depth of 3.4 cm from the surface (distance from the hotspot to the tumor location). The digital model consisted of point clouds of random spatial points from various regions of the breast, including the interior, surface, chest wall and from the surface temperatures registered data. The PINN model predicts the heat generation map in the tissue (indicative of metabolic activity) that applied the Pennes bioheat principle at the interior and adjusted for other predetermined confounding factors to detect the tumor characteristics if present.

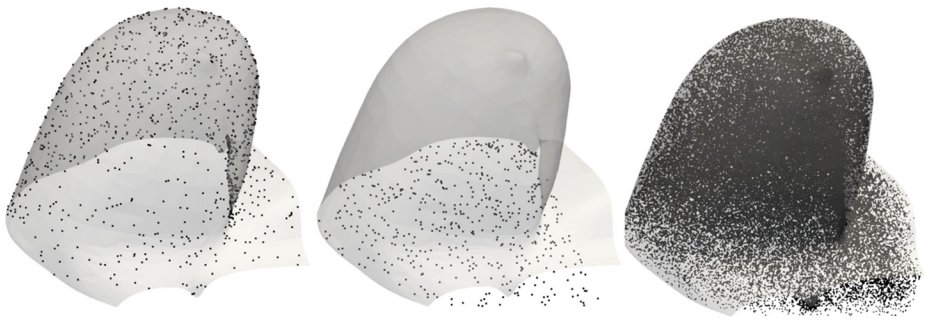

Fig. 3 Point clouds generated to define inputs to the PINN-SDSD of patient-8: (*a*) surface points, (*b*) chest points, and (*c*) interior points

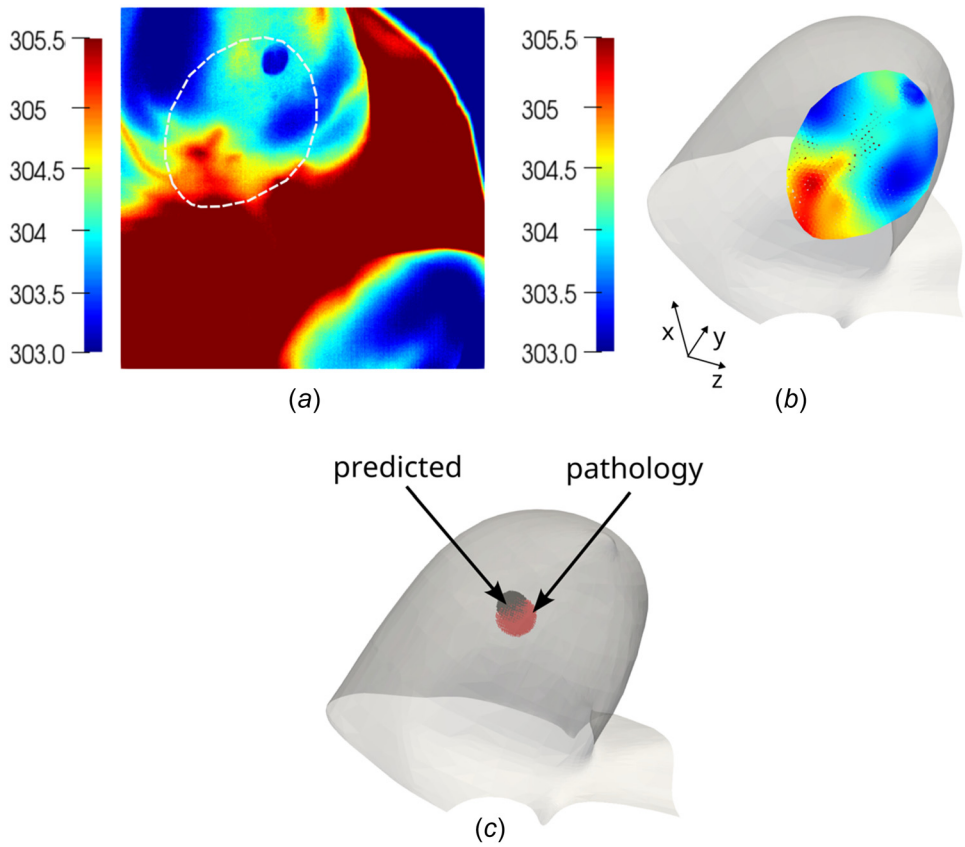

Fig. 4 Analysis of patient-8, (*a*) clinically reported infrared temperature, (*b*) PINN-SDSD predicted temperature, and (*c*) pathological and predicted tumor characteristics. In (*a*), the dashed circle indicates the predicted region shown by the PINN-SDSD. In (*c*), the black spot indicates the predicted tumor characteristics and red spot indicates the tumor characteristics in the pathology report.

Figure 4 shows the information corresponding to patient-8, including (a) the infrared temperature at the most predominant view, (b) the PINN predicted temperature at a predominant region, and (c) the tumor reported by pathology and the PINN prediction. The circle in Fig. 4(*a*) shows the region used for training. The infrared image in Fig. 4(*a*) shows abrupt changes in temperature creating isolated hotspots and cold regions. A comparison between the results in Figs. 4(*a*) and 4(*b*) shows that the PINN-SDSD effectively learned the pronounced variations in temperature capturing the sharp transitions from high to low temperatures. These results indicate that the use of three hidden layers with twenty neurons is an effective neural network configuration to capture the variation in temperature in the breast surface with cancerous tumor signature. The results in Fig. 4(*c*) indicate predicted smaller tumor located closer to the breast surface. The smaller tumors with higher heat generation lead to more pronounced hotspot regions over the surface. In addition, the PINN-SDSD places the tumor closer to the surface to compensate for the underestimation in the tumor size.

Figure 5 shows a regression analysis for quantification of the error between the prediction and the infrared temperatures. The error analysis considered a sample of $N = 50$ random points for comparison between the two data sets (predicted and infrared). The scaling of the temperatures allows effective quantification of the error. The results in Fig. 5 indicate that the PINN-SDSD closely reproduces the IR temperatures with an $R^2 = 0.98$. The prediction is accurate and only a few isolated points have a large error. The maximum error occurs at around 0.7 observed scaled infrared temperature. At this point, the predicted scaled infrared temperature is 0.83. A 0.7 scale temperature corresponds to 304.8 K and 0.83 scaled temperature corresponds to 305.13 K. The maximum error is then 0.33 K. These small errors are mainly driven by the noise in the infrared image and the ability of the PINN-SDSD to predict an output temperature free of noise.

Table 4 compares the predicted tumor location with the clinically detected tumor characteristics. The results show that PINN-SDSD accurately detected the tumor size and location. The PINN-SDSD predicted a smaller tumor and placed the tumor closer to the surface. Results show that the PINN-SDSD underestimates the tumor diameter by 0.4 cm and overestimates the location of the tumor by a maximum length of 0.3 cm. The predicted tumor has a depth of

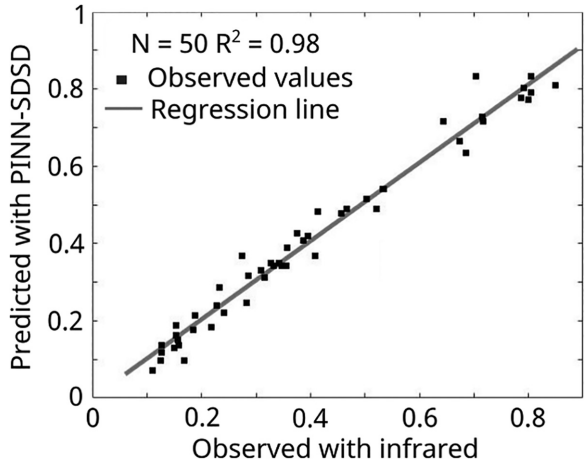

Fig. 5 Error quantification of the predicted PINN-SDSD relative to the IR temperatures

Table 4 Comparison of tumor characteristics pathology and predicted with PINN-SDSD

Analysis and error	d_0 (cm)	x_0 (cm)	y_0 (cm)	z_0 (cm)
Pathology	1.7	4.7	7.3	12.3
Predicted	1.3	4.77	7.6	12.0
Error	0.4	0.07	0.3	0.3

3.3 cm, which implies an underestimation of the tumor depth by 0.1 cm. These differences can be the result of errors in the registration between the digital breast model and the infrared image. Also, there is multiple possible solutions (e.g., larger tumors located deeper from the surface can generate same thermal signature as smaller tumors located closer to the surface). Still, the results show that the breast surface curvature and the temperature variation in the infrared image give enough information to constrain the predicted tumor characteristic to a tumor that closely resembles the tumor in the pathology report.

5 Limitations

Testing with one patient demonstrated the use of PINNs in simultaneously performing inverse modeling and forward modeling to find the tumor characteristics that satisfy the governing equations, boundary conditions, and infrared data. However, testing with more datasets is required to investigate the feasibility of the proposed approach. Additional testing may consider computer modeling or with in vitro experiments. Computer modeling creates scenarios where the Pennes bioheat equation drives the thermal transport, which can help with identifying the limits in terms of tumor diameter and depth. In-vitro experiments with localized heat sources embedded in 3D-printed plastic breasts can also contribute to improving the overall detection system including the positioning of the infrared camera. Also, identifying the performance of the PINN-SDSD with dynamic infrared is a relevant aspect to explore since it may improve the performance in terms of accuracy or detectability limits. Moreover, recent studies show that dynamic infrared imaging may contribute to identify the effect of internal vasculature on the tumor signature on the breast surface [55].

The proposed PINN-SDSD approach accurately detects the tumor by predicting tumor characteristics that closely match the results in the pathology report. The results indicated small errors of 0.4 cm in the predicted tumor diameter and 0.3 cm in the predicted tumor location. However, testing with additional patient datasets is required to identify if the PINN-SDSD can work with patients of different tissue densities or breast morphologies. The application of the PINN-SDSD to twenty datasets will allow the quantification of the standard deviation in the predicted characteristics. Testing additional patients will allow identifying the performance of the proposed approach in terms of specificity and sensitivity for comparison with other available techniques.

Optimization of the PINN-SDSD by reducing the training time and ensuring an accurate prediction will allow a more effective and robust tumor detection algorithm. The number of points in the point-clouds needs to be varied to investigate the influence on the performance. In addition, it is important to consider the number of training iterations during the searching of the tumor location as well as utilizing multiple graphics processing units simultaneously to reduce the training time.

6 Conclusions

The present work demonstrated the use of a physics-informed neural network to detect sources with surface data (PINN-SDSD). The developed PINN-SDSD detected a tumor in a patient with biopsy-proven breast cancer by training with surface infrared images and the equations of thermal transport. The PINN-SDSD has a fully connected neural network with spatial coordinates of points as inputs and the temperature at these points as outputs. The machine learning model finds the optimal relation between the inputs and output by minimizing losses defined based on the boundary conditions, the Pennes bioheat equation governing the thermal transport, and the infrared temperatures. In the PINN-SDSD, the perfusion rate and metabolic heat generation in the Pennes bioheat equation are expressed in terms of the tumor characteristics (location and size). By minimizing the losses during the training, the PINN-SDSD finds the optimal values of the tumor characteristics that satisfy the physics equations, boundary conditions, and infrared data. Generating point-clouds considered a digital breast model obtained from MRI images. At the Rochester General Hospital, the patient underwent MRI and infrared imaging in the prone position to facilitate the registration between the two image datasets.

The PINN-SDSD accurately identified the solution that satisfies the Pennes bioheat equation, boundary conditions, and infrared temperatures. The neural network captured the larger variations in temperature in breast surface regions with hotspots (from the tumor heat generation) and cold regions (near the nipple and other regions with high curvature). The predicted temperatures matched the infrared temperatures with a coefficient of determination $R^2 = 0.98$. Moreover, the PINN-SDSD detected a tumor that closely resembled the tumor specified in the pathology report. The highest absolute errors were 0.4 cm in the predicted tumor diameter and 0.3 cm in the identified location. These results indicate that the PINN-SDSD detects cancerous tumors and achieves an acceptable prediction of the tumor size and location.

Significant developments are required to establish the feasibility of the PINN-SDSD as a preferred adjunct technology. The machine learning algorithm needs improvements to reduce the training time, which can be done by evaluating the effect of the number of points, training iterations, and the use of multiple graphics processing units. Other relevant areas of development lie in the infrared camera position to improve the registration or the development of alternative approaches to generate precise thermal-spatial point clouds independently from MRI images. Testing with additional patients will allow identifying the uncertainty in the prediction of the tumor characteristics and will contribute to quantifying the sensitivity and specificity of the proposed machine learning approach.

Funding Data

- National Science Foundation (NSF) (Grant No. 2136325; Funder ID: 10.13039/100000001).

Conflict of Interest

The authors declare the following financial interests/personal relationships which may be considered as potential competing interests: Kandlikar reports equity position in BiRed Imaging.

Data Availability Statement

The datasets generated and supporting the findings of this article are obtainable from the corresponding author upon reasonable request.

References

[1] Ahmad, A., ed., 2019, *Breast Cancer Metastasis and Drug Resistance: Challenges and Progress*, Springer, Cham, Switzerland.

[2] American Cancer Society, 2022, "Cancer Facts & Figures," American Cancer Society, Atlanta , GA, accessed June 20, 2023, https://www.cancer.org/research/cancer-facts-statistics/all-cancer-facts-figures/cancer-facts-figures-2022.html

[3] Shafiq, A., Çolak, A. B., Sindhu, T. N., Lone, S. A., and Abushal, T. A., 2023, "Modeling and Survival Exploration of Breast Carcinoma: A Statistical, Maximum Likelihood Estimation, and Artificial Neural Network Perspective," Artif. Intell. Life Sci., **4**, p. 100082.

[4] Narod, S. A., Iqbal, J., and Miller, A. B., 2015, "Why Have Breast Cancer Mortality Rates Declined?," J. Cancer Policy, **5**, pp. 8–17.

[5] Grabler, P., Sighoko, D., Wang, L., Allgood, K., and Ansell, D., 2017, "Recall and Cancer Detection Rates for Screening Mammography: Finding the Sweet Spot," Am. J. Roentgenol., **208**(1), pp. 208–213.
[6] Lehman, C. D., Arao, R. F., Sprague, B. L., Lee, J. M., Buist, D. S. M., Kerlikowske, K., Henderson, L. M., et al., 2017, "National Performance Benchmarks for Modern Screening Digital Mammography: Update From the Breast Cancer Surveillance Consortium," Radiology, **283**(1), pp. 49–58.
[7] Nelson, H. D., Pappas, M., Cantor, A., Griffin, J., Daeges, M., and Humphrey, L., 2016, "Harms of Breast Cancer Screening: Systematic Review to Update the 2009 U.S. Preventive Services Task Force Recommendation," Ann. Intern. Med., **164**(4), pp. 256–267.
[8] Gonzalez-Hernandez, J.-L., Recinella, A. N., Kandlikar, S. G., Dabydeen, D., Medeiros, L., and Phatak, P., 2020, "An Inverse Heat Transfer Approach for Patient-Specific Breast Cancer Detection and Tumor Localization Using Surface Thermal Images in the Prone Position," Infrared Phys. Technol., **105**, p. 103202.
[9] Sritharan, N., Gutierrez, C., Perez-Raya, I., Gonzalez-Hernandez, J.-L., Owens, A., Dabydeen, D., Medeiros, L., Kandlikar, S. G., and Phatak, P., 2023, "Abstract PO1-07-12: Inverse Modeling With Surface Temperature Accurately Detects the Presence of Breast Cancer," Cancer Res., **84**(9_Supplement), p. PO1-07-12.
[10] Gutierrez, C., Owens, A., Medeiros, L., Dabydeen, D., Sritharan, N., Phatak, P., and Kandlikar, S. G., 2024, "Breast Cancer Detection Using Enhanced IRI-Numerical Engine and Inverse Heat Transfer Modeling: Model Description and Clinical Validation," Sci. Rep., **14**(1), p. 3316.
[11] Cai, S., Wang, Z., Wang, S., Perdikaris, P., and Karniadakis, G. E., 2021, "Physics-Informed Neural Networks for Heat Transfer Problems," ASME J. Heat Mass Transfer-Trans. ASME, **143**(6), p. 060801.
[12] Oommen, V., and Srinivasan, B., 2022, "Solving Inverse Heat Transfer Problems Without Surrogate Models: A Fast, Data-Sparse, Physics Informed Neural Network Approach," ASME J. Comput. Inf. Sci. Eng., **22**(4), p. 041012.
[13] Jagtap, N. V., Mudunuru, M. K., and Nakshatrala, K. B., 2023, "CoolPINNs: A Physics-Informed Neural Network Modeling of Active Cooling in Vascular Systems," Appl. Math. Modell., **122**, pp. 265–287.
[14] Zhang, B., Wu, G., Gu, Y., Wang, X., and Wang, F., 2022, "Multi-Domain Physics-Informed Neural Network for Solving Forward and Inverse Problems of Steady-State Heat Conduction in Multilayer Media," Phys. Fluids, **34**(11), p. 116116.
[15] Perez-Raya, I., and Kandlikar, S. G., 2023, "Thermal Modeling of Patient-Specific Breast Cancer With Physics-Based Artificial Intelligence," ASME J. Heat Mass Transfer-Trans. ASME, **145**(3), p. 031201.
[16] Cuomo, S., Di Cola, V. S., Giampaolo, F., Rozza, G., Raissi, M., and Piccialli, F., 2022, "Scientific Machine Learning Through Physics–Informed Neural Networks: Where We Are and What's Next," J. Sci. Comput., **92**(3), p. 88.
[17] Kollmannsberger, S., D'Angella, D., Jokeit, M., and Herrmann, L., 2021, *Deep Learning in Computational Mechanics, An Introductory Course*, Springer International Publishing, Cham.
[18] Raissi, M., Perdikaris, P., and Karniadakis, G. E., 2017, "Inferring Solutions of Differential Equations Using Noisy Multi-Fidelity Data," J. Comput. Phys., **335**, pp. 736–746.
[19] Raissi, M., Perdikaris, P., and Karniadakis, G. E., 2017, "Machine Learning of Linear Differential Equations Using Gaussian Processes," J. Comput. Phys., **348**, pp. 683–693.
[20] Raissi, M., Ramezani, N., and Seshaiyer, P., 2019, "On Parameter Estimation Approaches for Predicting Disease Transmission through Optimization, Deep Learning and Statistical Inference Methods," Lett. Biomath., **6**(2), pp. 1–26.
[21] Raissi, M., and Karniadakis, G. E., 2018, "Hidden Physics Models: Machine Learning of Nonlinear Partial Differential Equations," J. Comput. Phys. **357**, pp. 125–141.
[22] Raissi, M., Perdikaris, P., and Karniadakis, G. E., 2018, "Numerical Gaussian Processes for Time-Dependent and Nonlinear Partial Differential Equations," SIAM J. Sci. Comput., **40**(1), pp. A172–A198.
[23] Karniadakis, G. E., Kevrekidis, I. G., Lu, L., Perdikaris, P., Wang, S., and Yang, L., 2021, "Physics-Informed Machine Learning," Nat. Rev. Phys., **3**(6), pp. 422–440.
[24] Dissanayake, M. W. M. G., and Phan-Thien, N., 1994, "Neural-Network-Based Approximations for Solving Partial Differential Equations," Commun. Numer. Methods Eng., **10**(3), pp. 195–201.
[25] Lagaris, I. E., Likas, A., and Fotiadis, D. I., 1998, "Artificial Neural Networks for Solving Ordinary and Partial Differential Equations," IEEE Trans. Neural Networks, **9**(5), pp. 987–1000.
[26] Lagaris, I. E., Likas, A. C., and Papageorgiou, D. G., 2000, "Neural-Network Methods for Boundary Value Problems With Irregular Boundaries," IEEE Trans. Neural Networks, **11**(5), pp. 1041–1049.
[27] Goodfellow, I., Bengio, Y., and Courville, A., 2016, *Deep Learning*, The MIT Press, Cambridge, MA.
[28] Dhall, D., Kaur, R., and Juneja, M., 2020, "Machine Learning: A Review of the Algorithms and Its Applications," *Proceedings of ICRIC 2019*, edited by P. K. Singh, A. K. Kar, Y. Singh, M. H. Kolekar, and S. Tanwar (Springer International Publishing, Cham), pp. 47–63.
[29] Dong, S., Wang, P., and Abbas, K., 2021, "A Survey on Deep Learning and Its Applications," Comput. Sci. Rev., **40**, p. 100379.
[30] Cai, S., Mao, Z., Wang, Z., Yin, M., and Karniadakis, G. E., 2021, "Physics-Informed Neural Networks (PINNs) for Fluid Mechanics: A Review," Acta Mech. Sin., **37**(12), pp. 1727–1738.
[31] Pashaei Kalajahi, A., Perez-Raya, I., and D'Souza, R. M., 2022, "Physics Informed Deep Neural Net Inverse Modeling for Estimating Model Parameters in Permeable Porous Media Flows," ASME J. Fluids Eng., **144** (6), p. 061102.
[32] Jambunathan, K., Hartle, S. L., Ashforth-Frost, S., and Fontama, V. N., 1996, "Evaluating Convective Heat Transfer Coefficients Using Neural Networks," Int. J. Heat Mass Transfer, **39**(11), pp. 2329–2332.
[33] Aliakbari, M., Mahmoudi, M., Vadasz, P., and Arzani, A., 2022, "Predicting High-Fidelity Multiphysics Data From Low-Fidelity Fluid Flow and Transport Solvers Using Physics-Informed Neural Networks," Int. J. Heat Fluid Flow, **96**, p. 109002.
[34] Wang, T., Wang, Z., Huang, Z., and Xi, G., 2022, "Multi-Domain Physics-Informed Neural Network for Solving Heat Conduction and Conjugate Natural Convection With Discontinuity of Temperature Gradient on Interface," Sci. China Technol. Sci., **65**(10), pp. 2442–2461.
[35] Go, M.-S., Lim, J. H., and Lee, S., 2023, "Physics-Informed Neural Network-Based Surrogate Model for a Virtual Thermal Sensor With Real-Time Simulation," Int. J. Heat Mass Transfer, **214**, p. 124392.
[36] Pratama, D. A., Bakar, M. A., Ibrahim, N. F., Idris, R., and Mohamed, N., 2023, "Physical Restriction Neural Networks With Restarting Strategy for Solving Mathematical Model of Thermal Heat Equation for Early Diagnose Breast Cancer," Results Appl. Math., **19**, p. 100384.
[37] Waring, J., Lindvall, C., and Umeton, R., 2020, "Automated Machine Learning: Review of the State-of-the-Art and Opportunities for Healthcare," Artif. Intell. Med., **104**, p. 101822.
[38] Arzani, A., Wang, J.-X., Sacks, M. S., and Shadden, S. C., 2022, "Machine Learning for Cardiovascular Biomechanics Modeling: Challenges and Beyond," Ann. Biomed. Eng., **50**(6), pp. 615–627.
[39] Nolte, D., and Bertoglio, C., 2022, "Inverse Problems in Blood Flow Modeling: A Review," Int. J. Numer. Methods Biomed. Eng., **38**(8), p. e3613.
[40] Fathi, M. F., Perez-Raya, I., Baghaie, A., Berg, P., Janiga, G., Arzani, A., and D'Souza, R. M., 2020, "Super-Resolution and Denoising of 4D-Flow MRI Using Physics-Informed Deep Neural Nets," Comput. Methods Programs Biomed., **197**, p. 105729.
[41] Habibi, M., D'Souza, R. M., Dawson, S. T. M., and Arzani, A., 2021, "Integrating Multi-Fidelity Blood Flow Data With Reduced-Order Data Assimilation," Comput. Biol. Med., **135**, p. 104566.
[42] Moser, P., Fenz, W., Thumfart, S., Ganitzer, I., and Giretzlehner, M., 2023, "Modeling of 3D Blood Flows With Physics-Informed Neural Networks: Comparison of Network Architectures," Fluids, **8**(2), p. 46.
[43] Perez-Raya, I., Fathi, M. F., Baghaie, A., Sacho, R. H., Koch, K. M., and D'Souza, R. M., 2020, "Towards Multi-Modal Data Fusion for Super-Resolution and Denoising of 4D-Flow MRI," Int. J. Numer. Methods Biomed. Eng., **36**(9), p. e3381.
[44] Zhang, X., Mao, B., Che, Y., Kang, J., Luo, M., Qiao, A., Liu, Y., et al., 2023, "Physics-Informed Neural Networks (PINNs) for 4D Hemodynamics Prediction: An Investigation of Optimal Framework Based on Vascular Morphology," Comput. Biol. Med., **164,** p. 107287.
[45] Sel, K., Mohammadi, A., Pettigrew, R. I., and Jafari, R., 2023, "Physics-Informed Neural Networks for Modeling Physiological Time Series for Cuffless Blood Pressure Estimation," Npj Digit. Med., **6**(1), pp. 1–15.
[46] Sarabian, M., Babaee, H., and Laksari, K., 2022, "Physics-Informed Neural Networks for Brain Hemodynamic Predictions Using Medical Imaging," IEEE Trans. Med. Imaging, **41**(9), pp. 2285–2303.
[47] Pennes, H. H., 1948, "Analysis of Tissue and Arterial Blood Temperatures in the Resting Human Forearm," J. Appl. Physiol., **1**(2), pp. 93–122.
[48] Mashekova, A., Zhao, Y., Ng, E. Y. K., Zarikas, V., Fok, S. C., and Mukhmetov, O., 2022, "Early Detection of the Breast Cancer Using Infrared Technology – a Comprehensive Review," Therm. Sci. Eng. Prog., **27**, p. 101142.
[49] Gonzalez-Hernandez, J.-L., Kandlikar, S. G., Dabydeen, D., Medeiros, L., and Phatak, P., 2018, "Generation and Thermal Simulation of a Digital Model of the Female Breast in Prone Position," J. Eng. Sci. Med. Diagn. Ther., **1**(4), p. 041006.
[50] Gonzalez-Hernandez, J.-L., Recinella, A. N., Kandlikar, S. G., Dabydeen, D., Medeiros, L., and Phatak, P., 2019, "Technology, Application and Potential of Dynamic Breast Thermography for the Detection of Breast Cancer," Int. J. Heat Mass Transfer, **131**, pp. 558–573.
[51] Kandlikar, S. G., Perez-Raya, I., Raghupathi, P. A., Gonzalez-Hernandez, J.-L., Dabydeen, D., Medeiros, L., and Phatak, P., 2017, "Infrared Imaging Technology for Breast Cancer Detection – Current Status, Protocols and New Directions," Int. J. Heat Mass Transfer, **108**, pp. 2303–2320.
[52] Lozano, A., Hayes, J. C., Compton, L. M., Azarnoosh, J., and Hassanipour, F., 2020, "Determining the Thermal Characteristics of Breast Cancer Based on High-Resolution Infrared Imaging, 3D Breast Scans, and Magnetic Resonance Imaging," Sci. Rep., **10**(1), p. 10105.
[53] Gautherie, M., 1980, "Thermopathology of Breast Cancer: Measurement and Analysis of In Vivo Temperature and Blood Flow," Ann. N. Y. Acad. Sci., **335**(1), pp. 383–415.
[54] Duck, F. A., 2013, *Physical Properties of Tissues: A Comprehensive Reference Book*, Academic Press, London, UK.
[55] Gershenson, M., and Gershenson, J., 2023, "Dynamic Vascular Imaging Using Active Breast Thermography," Sensors, **23**(6), p. 3012.